IEEE Robotics and Automation Letters (RA-L) paper, presented at ICRA 2026, Vienna, Austria. Cite as RA-L paper.

Actuator Dynamics-Aware Model Predictive Control of a Wheeled Inverted Pendulum with a Fan

Dohyeon Kim and Yeongtae Jung, *Member, IEEE*

***Abstract*—Wheeled Inverted Pendulum (WIP) systems offer agile mobility but are challenging to control due to their unstable and underactuated dynamics. To address these limitations, we develop a Wheeled Inverted Pendulum with a Fan (WIPF), which incorporates a fan-generated bidirectional thrust force as an additional control input. This makes the system fully actuated and enhances stability; however, the limited bandwidth of the fan thrust introduces control challenges. In this letter, we propose a Frequency-Shaped Model Predictive Control (FSMPC) design framework that accounts for actuator dynamics in the optimization process, and is expandable to other systems with different actuator dynamics. The proposed FSMPC can provide improved stability by penalizing high-frequency input using the frequency response of the fan. The nonlinear solver enables control input updates at rates exceeding 1 kHz, meeting real-time control requirements. The performance of FSMPC with the proposed design framework is compared through simulations and experiments against a Linear Quadratic Regulator (LQR), a standard Model Predictive Controller (MPC), and a Frequency-Shaped LQR (FSLQR) that does not consider fan dynamics or the input constraint. The results demonstrate that FSMPC achieves improved stability and robustness compared to other controllers.**

***Index Terms*—Actuation and joint mechanisms, optimization and optimal control, motion control.**

I. Introduction

WHEELED inverted pendulum (WIP) robots have been widely researched due to their agile locomotion and effective mobility across various environments [1], [2], [3]. Various control strategies, including whole-body controllers [4] and model-free controllers [5], have been employed to stabilize and control WIP and legged WIP systems [6], [7], [8]. However, WIP systems remain challenging to control due to their inherently unstable and underactuated dynamics. Their dependence on ground reaction forces makes them unstable on low-friction or uneven surfaces, while their non-minimum phase behavior limits motion in constrained spaces. To overcome these limitations of traditional WIP systems, additional balancing mechanisms have been explored. Air blowers have been utilized to control roll motion in [9], [10], while the pitch control relies on wheel torque as same as traditional WIPs, inheriting the same drawbacks in sagittal plane dynamics. Reaction wheels [11] and control moment gyros [12] provide pitch stabilization but require heavy rotating masses and are constrained by wheel and gimbal speed saturation.

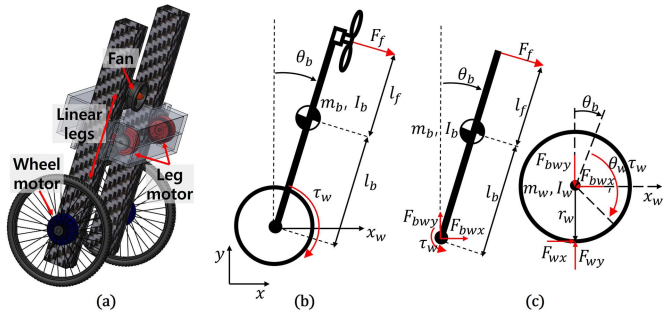

Fig. 1. (a) Concept of the WIPF robot. (b) A 2D reduced model of the WIPF. (c) Free body diagram of the WIPF.

We are developing a robot that incorporates a wheeled inverted pendulum with a fan (WIPF) along with linear legs to achieve agile motion over various terrain (Fig. 1(a)). The bidirectional fan functioning in the sagittal plane allows fully actuated characteristics; thus, the tilting and locomotion can be separately controlled. This also enables balance over low-friction terrain as the thrust is independent of terrain conditions. The linear leg mechanism allows for height adjustment without interfering with the environment, making it suitable for use in limited spaces. A simplified model with a wheel, a fan, and the body was introduced in our previous work and controlled by a simple linear quadratic regulator (LQR) [13]. This was the first WIP system to implement bidirectional thrust with a fan in the pitch direction, whereas only unidirectional thrust was utilized in [14]. However, controlling fan-actuated systems is challenging due to the fan's limited thrust bandwidth (a few hertz) and asymmetric thrust behavior resulting in highly nonlinear actuator dynamics. On the other hand, the wheel motor offers a much higher bandwidth (hundreds of hertz), resulting in a hybrid actuation system that increases the complexity to the controller design.

Received 3 March 2025; accepted 15 June 2025. Date of publication 2 July 2025; date of current version 7 July 2025. This article was recommended for publication by Associate Editor S. Han and Editor C. Della Santina upon evaluation of the reviewers' comments. This work was supported by the National Research Foundation of Korea(NRF) through the Korea Government(MSIT) under Grant RS-2022-00166825. *(Corresponding author: Yeongtae Jung.)*

Dohyeon Kim is with the Graduate school of Mechanical-Aerospace-Electric Convergence Engineering, Jeonbuk National University, Jeonju 54896, South Korea.

Yeongtae Jung is with the Graduate school of Mechanical-Aerospace-Electric Convergence Engineering, Jeonbuk National University, Jeonju 54896, South Korea, also with the Department of Mechanical System Engineering, Jeonbuk National University, Jeonju 54896, South Korea, and also with the Advanced Transportation Machinery Research Center, Jeonbuk National University, Jeonju 54896, South Korea (e-mail: ytjung@jbnu.ac.kr).

This article has supplementary downloadable material available at https://doi.org/10.1109/LRA.2025.3585391, provided by the authors.

Digital Object Identifier 10.1109/LRA.2025.3585391

Model Predictive Control (MPC) algorithms can be used for the optimal control of such a hybrid actuation system. MPC has demonstrated superior performance in trajectory optimization and tracking controller [15], [16], but its iterative nature imposes computational challenges for real-time control with the update rate of a few tens of hertz. Another limitation arises from the modeling uncertainty. In drone systems, for example, the nonlinear dynamics of fan motors and propellers are often neglected in low-level control, which results in modeling uncertainties [16], [17]. To address these uncertainties, integrators are commonly added to feedback controllers; however, this approach decreases both stability and bandwidth of the system. An alternative approach is to treat these uncertainties as disturbances and apply disturbance rejection control [18]. However, this requires time to observe the disturbance, resulting in a delayed response. While fan dynamics were considered as inequality constraints in the MPC controller in [19], these highly nonlinear constraints limited control frequency to 150–400 Hz, which is insufficient for two-wheeled or legged robotic systems that typically require 500–1000 Hz. Thus, it is necessary to develop fast real-time MPC that accounts for actuator dynamics, minimizing model complexity. Frequency-Shaped LQR (FSLQR) [20] can address such uncertainties induced by actuator dynamics via a frequency-dependent cost function; however, it cannot handle the system's nonlinearities or input constraints [21].

To overcome these limitations, Frequency-Shaped MPC (FSMPC) extends FSLQR to a constrained nonlinear MPC framework. Yun et al. proposed FSMPC in [22] with the application to a simulated second-order linear system. FSMPC was later applied to real-world robots in [23] to address challenges arising from variable contact dynamics, accounting for terrain-specific contact frequencies. However, this approach was used only for high-level trajectory optimization. The cost function was also designed in an empirical way by tuning the parameters manually.

We propose a systematic design process of the FSMPC to achieve real-time control of a nonlinear system considering the actuator output bandwidths of hybrid actuation systems. The dynamics of a fan in WIPF is identified through experiments and utilized to design a frequency-dependent cost function, allowing the controller to leverage fan thrust in the low-frequency range while using wheel torque over a wide frequency range. In this way, the force bandwidth of different actuators can be reflected to the controller. An SQP-based solver, which allows using nonlinear system models and inherently handles state and input constraints, was applied to reduce the model uncertainty.

The primary contributions of this research are:

- Investigation on the dynamics of a fan actuation system that can provide bidirectional thrust.
- Actuator dynamics-aware design framework for the frequency-dependent cost function of FSMPC, which can be applied in the low-level control for a high-speed real-time system.
- Simulational and experimental validation of the stability and robustness of the proposed FSMPC.

The remainder of this letter is structured as follows. Section II introduces the dynamics of the WIPF system. The design of the frequency-shaped MPC is presented in Section III. Sections IV and V validate the stability of the system with simulations and experiments, respectively. Finally, Section VI concludes with limitations and future plans.

TABLE I
PARAMETERS OF THE WIPF

Symbol	Quantity
F_f	Fan thrust
τ_w	Torque applied by the wheel motor
m_b	Mass of the robot body
I_b	Rotational inertia of the robot body
m_w	Mass of the wheel and the motor
I_w	Rotational inertia of the wheel and the motor
l_f	Distance between the fan and the CoM
l_b	Distance between the CoM and the wheel
θ_b	Pitch angle of the body
x_w	Distance traveled by the wheel
F_{bwx}	Reaction force along the x-axis applied on the axle
F_{bwy}	Reaction force along the y-axis applied on the axle
F_{wx}	Friction force along the x-axis at the contact point between the wheel and the ground
F_{wy}	Friction force along the y-axis at the contact point between the wheel and the ground

II. Dynamics of WIPF

The dynamics of WIPF is investigated in this section to understand its characteristics and to design FSMPC that can account for a hybrid actuation system with different input bandwidths.

A. Modeling

Fig. 1(b) shows the reduced model of the WIPF that incorporates additional input to the traditional WIP: bidirectional fan thrust [13]. The model is designed considering the sagittal plane dynamics assuming a constant leg length as this research focuses on navigating the control of hybrid actuation systems with different force bandwidths. The dynamics of WIPF can be derived using the Newton-Euler approach with the free body diagram shown in Fig. 1(c). The fan thrust, denoted as F_f is located above the center of mass (CoM), which includes the fan as well as all other structural components. Other configurations and notations are similar with traditional WIP systems. Detailed parameters are provided in Table I.

The rotation, horizontal and vertical translation of the body are governed by following equations.

$$I_b\ddot{\theta}_b = -\tau_w - F_{bwx}l_b\cos\theta_b + F_{bwy}l_b\sin\theta_b + F_f l_f \tag{1}$$

$$m_b\left(\ddot{x}_w + l_b(\ddot{\theta}_b\cos\theta_b - \dot{\theta}_b^2\sin\theta_b)\right) = F_{bwx} + F_f\cos\theta_b \tag{2}$$

$$m_b\left(l_b(-\ddot{\theta}_b\sin\theta_b - \dot{\theta}_b^2\cos\theta_b)\right) = F_{bwy} - m_b g - F_f\sin\theta_b \tag{3}$$

Similarly, the rotation, horizontal and vertical translation of the wheel can be expressed as follows:

$$I_w(\ddot{\theta}_b + \ddot{\theta}_w) = \tau_w - F_{wx}r_w \tag{4}$$

$$m_w\ddot{x}_w = F_{wx} - F_{bwx} \tag{5}$$

$$-F_{bwy} + F_{wy} - m_w g = 0 \tag{6}$$

IEEE Robotics and Automation Letters (RA-L) paper, presented at ICRA 2026, Vienna, Austria. Cite as RA-L paper.

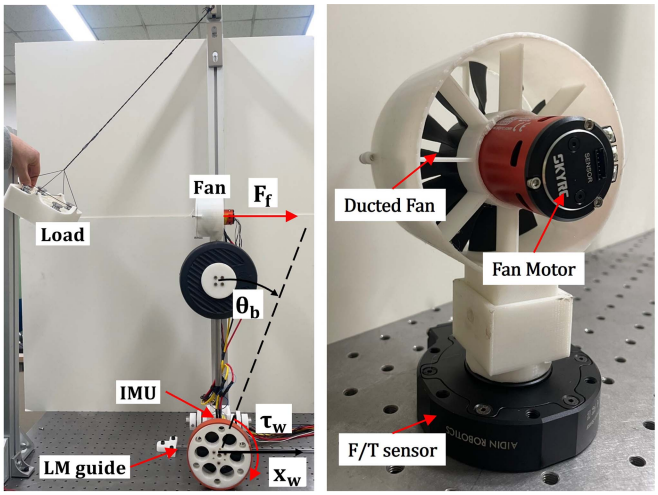

Fig. 2. Prototype testbed of the WIPF. (a) Overall configurations. (b) Fan system identification setup.

Assuming non-slip condition, the rolling constraint between the wheel and the ground can be expressed as follows:

$$\ddot{x}_w = r_w(\ddot{\theta}_b + \ddot{\theta}_w) \tag{7}$$

Combining (1)–(7) results two governing equations as follows:

$$\ddot{x}_w\left(m_b + m_w + \frac{I_w}{r_w^2}\right) + m_b l_b(\ddot{\theta}_b \cos\theta_b - \dot{\theta}_b^2 \sin\theta_b) = \frac{\tau_w}{r_w} + F_f \cos\theta_b \tag{8}$$

$$m_b l_b \cos\theta_b \ddot{x}_w + \left(m_b l_b^2 + I_b\right)\ddot{\theta}_b - m_b g l_b \sin\theta_b = (l_b + l_f)F_f - \tau_w \tag{9}$$

Note that the two control inputs, wheel torque τ_w and the fan thrust F_f allow the system to be fully actuated, whereas a traditional WIP that does not have F_f is underactuated. Model-based controllers can effectively be used to control this system based on the derived governing equations. However, a problem arises from the dynamics of the fan, which limits the bandwidth of F_f.

B. Fan Dynamics

A prototype testbed built in [13] (Fig. 2), was used to investigate the WIPF dynamics and test the controller, which will be developed in Section III. A back-drivable quasi-direct drive motor that can provide output torque bandwidth up to around a hundred hertz was used for the wheel actuation. The position and velocity of the wheel motor are transmitted to the controller, which runs at 1 kHz via CAN bus. A ducted fan with a BLDC motor is mounted on top of the WIPF body to generate fan thrust. We used a Hall sensor-equipped BLDC motor and a bidirectional controller to achieve continuous bidirectional thrust with a single fan, which is uncommon in drone applications. A 1.5 kg weight is placed between the fan and the motor. An inertial measurement unit (IMU) is positioned near the motor to measure the tilt angle and angular velocity of the body. To minimize slip during these experiments, high-friction tape was applied to the wheel. While this does not fully guarantee ideal non-slip conditions, it reflects the real-world conditions in the practical application of WIPF robots. Detailed hardware specifications are summarized in Table II.

TABLE II
HARDWARE SPECIFICATIONS OF THE WIPF SYSTEM

Component	Specification
Wheel motor	CubeMars AK 80-6 Rated torque: 6 Nm Peak torque: 12 Nm Encoder resolution: 14 bit
Fan motor	SKY RC Cheetah 1/10-1870KV Rated current: 60 A Hall sensor embedded
Electronic speed controller (ESC)	ODrive v3.6 Rated current: 60 A Reference signal: 500 Hz PWM
Controller	National Instruments cRIO-9082 Control rate: 1 kHz FPGA clock: 40 MHz Modules: NI-9853 and NI-9401
IMU sensor	EBmotion-V5 Maximum sensing rate: 1 kHz

The fan dynamics can be modeled considering the aerodynamic properties, inertia, and the control diagram of the electric speed controller (ESC). It is well known that the fan thrust shows a linear relationship with the square of fan speed as follows:

$$F_f = k_{thrust}\dot{\theta}_f^2 \tag{10}$$

where F_f is the fan thrust force, k_{thrust} represents the thrust coefficient, and $\dot{\theta}_f$ represents the fan speed. Considering the inertia and drag force of the fan and rotor [24], [25], and internal PI speed controller of the electronic speed controller (ESC) [26], we can derive the equation of motion of the fan as follows:

$$I\ddot{\theta}_f + k_{drag}\dot{\theta}_f^2 = k_t\left(k_i \int e\, dt + k_p e\right) \tag{11}$$

where I is the inertia of the fan and rotor, k_{drag} is the drag constant, k_t, k_p, and k_i represents the torque constant of the motor, proportional and integral gain of the PI controller of the ESC, respectively. e is defined as follows:

$$e = \dot{\theta}_{f,ref} - \dot{\theta}_f \tag{12}$$

where $\theta_{f,ref}$ is the reference fan speed. Equation (10) and (11) represent the closed-loop controlled fan dynamics.

The thrust coefficient was identified by measuring the actual output force using the force/torque sensor shown in Fig. 2(b) for several fan velocities at the steady state of each stair of a staircase fan velocity profile (Fig. 3(a)). The k_{thrust} for the forward direction was $6.169 \times 10^{-6}\,\text{N}\cdot\text{s}^2$, while that for the reverse direction was $3.955 \times 10^{-6}\,\text{N}\cdot\text{s}^2$. The maximum forces in those directions were 3.74 N and -2.35 N, respectively. The drag coefficient was identified with a quasi-static sinusoidal desired thrust force input at 0.01 Hz with an amplitude of 1 N over 100 seconds, assuming that the inertia does not

IEEE Robotics and Automation Letters (RA-L) paper, presented at ICRA 2026, Vienna, Austria. Cite as RA-L paper.

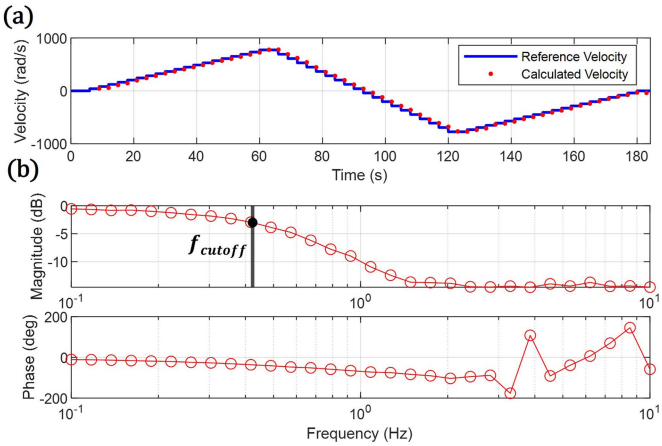

Fig. 3. Fan identification results. (a) Reference and calculated velocity using identified k_{thrust}. (b) Frequency response of the fan.

affect the dynamics ($k_{drag,forward} = 2.946 \times 10^{-8}\,\mathrm{N \cdot m \cdot s^2}$, $k_{drag,reverse} = 1.392 \times 10^{-8}\,\mathrm{N \cdot m \cdot s^2}$). The rotor and fan inertia was identified to $2.494 \times 10^{-5}\,\mathrm{kg \cdot m^2}$ from a step response with a desired velocity equal to the maximum available velocity magnitude.

The frequency response of the closed-loop controlled fan was tested to determine its dynamic characteristics and identify the remaining unidentified system parameter in (11). Reference fan velocity trajectories for a 1 N amplitude sinusoidal bidirectional desired thrust were applied to the fan driver, with the frequency varying from 0.1 Hz to 2.5 Hz. The actual fan velocity was measured simultaneously. Fig. 3 shows the bidirectional frequency response of the fan velocity. Note that the controlled fan has a cutoff frequency of 0.4234 Hz, significantly slower than the wheel motor torque bandwidth, which operates in the hundreds of hertz. These limited-force-bandwidth dynamics are typically ignored in most applications, particularly for multirotors, and consequently it negatively affects stability and control accuracy [17], [18], [19]. Therefore, it is essential to incorporate the fan's dynamic characteristics in the controller design to ensure stability by reducing modeling uncertainty.

III. Controller

MPC is widely used to control robotic systems, as it provides optimal control inputs based on given cost functions and system models. However, introducing complex nonlinear systems, such as fan dynamics, increases computational burdens and makes it difficult to apply in real-time control systems. This research develop a nonlinear model predictive controller (NMPC) with a frequency-shaped cost function [20] to provide optimal control input in real-time. For this, we propose a systematic design framework of the frequency-shaped cost function that accounts for the limited bandwidth of actuator dynamics.

A typical quadratic cost function in the time domain is expressed as follows:

$$J = \frac{1}{2}\int_0^\infty \left(x^T(t)Qx(t) + \rho u^T(t)Ru(t)\right)dt \tag{13}$$

where $x(t)$ is the state of the system, Q is the weighting matrix for the state, ρ is the scaling factor, $u(t)$ is the input for the desired fan thrust, R is the weighting matrix for the input. This equation can be converted to frequency domain using the Fourier transform as follows:

$$J = \frac{1}{2}\int_{-\infty}^\infty \left(X^T(j\omega)QX(j\omega) + \rho U^*(j\omega)RU(j\omega)\right)d\omega \tag{14}$$

Since the control objective is to manage slow actuator dynamics with frequency-dependent output force, it is intuitive that the control weighting matrix R should be generalized as a frequency-dependent function:

$$R(j\omega) = R_f^*(j\omega)R_f(j\omega) > 0 \tag{15}$$

where * denotes complex conjugate transpose. Then, the cost function in the frequency domain becomes as follows:

$$J = \frac{1}{2}\int_{-\infty}^\infty \left(X^T(j\omega)QX(j\omega) + \rho U^*(j\omega)R(j\omega)U(j\omega)\right)d\omega \tag{16}$$

To make $R(j\omega)$ usable in the time domain, we can use $R_f(j\omega)$ as a filter, allowing the relationship between $U(j\omega)$ and the filtered control input $U_f(j\omega)$ to be satisfied as:

$$U_f(j\omega) = R_f(j\omega)U(j\omega) \tag{17}$$

Substituting this into the cost function gives a new cost function composed of the filtered input variables as follows:

$$J = \frac{1}{2}\int_{-\infty}^\infty \left(X^T(j\omega)QX(j\omega) + \rho U_f^*(j\omega)U_f(j\omega)\right)d\omega \tag{18}$$

Using Parseval's theorem, this can be transformed back into the time domain as follows:

$$J = \frac{1}{2}\int_0^\infty \left(x^T(t)Qx(t) + \rho u_f^T(t)u_f(t)\right)dt \tag{19}$$

However, the quadratic function involving the filtered control inputs is still difficult to solve. Therefore, it is necessary to convert it into a standard quadratic problem. The frequency-shaping weighting transfer function, R_f, can be expressed using state-space realization:

$$\dot{z}_1(t) = A_1 z_1(t) + B_1 u(t) \tag{20}$$

$$u_f(t) = C_1 z_1(t) + D_1 u(t) \tag{21}$$

An intermediate state z_1 is introduced. By substituting (21) into (19), the cost function can be expressed as:

$$J = \frac{1}{2}\int_0^\infty \left(x^T Qx + \rho(C_1 z_1 + D_1 u)^T(C_1 z_1 + D_1 u)\right)dt. \tag{22}$$

The resulting nonlinear system dynamics are:

$$\begin{bmatrix}\dot{x}\\ \dot{z}_1\end{bmatrix} = \begin{bmatrix}f(x,u,t)\\ A_1 z_1 + B_1 u\end{bmatrix} \tag{23}$$

Since the fan thrust input exhibits relatively slow dynamic characteristics, the weighting function $R_f(j\omega)$ can be designed

IEEE Robotics and Automation Letters (RA-L) paper, presented at ICRA 2026, Vienna, Austria. Cite as RA-L paper.

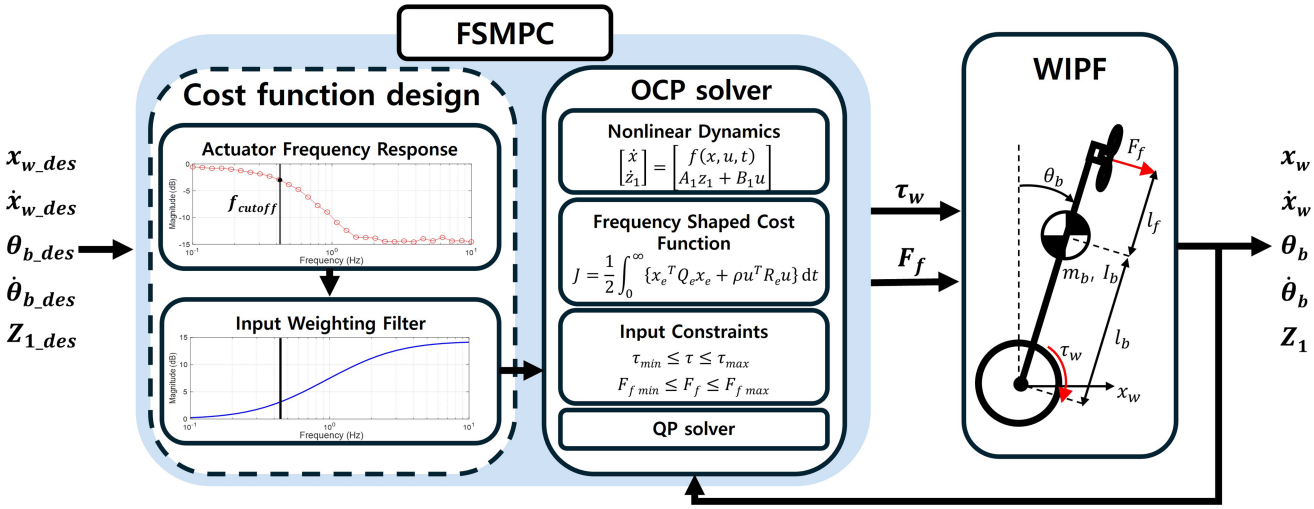

Fig. 4. Overall controller architecture of FSMPC for the WIPF system with the design framework. The fan's frequency response is utilized to design an input weighting filter for the frequency-dependent cost function. The OCP solver processes this information to output motor wheel torques and fan thrust, explicitly accounting for the fan's dynamic characteristics.

to penalize high-frequency fan control inputs as follows:

$$R(j\omega) = R_f^*(j\omega)R_f(j\omega) = \left|\frac{1+\alpha j\omega}{1+\beta j\omega}\right|^2 \tag{24}$$

The parameters α and β determine the frequency-dependent penalty, which were set in an empirical way in previous researches. The parameters were selected by comparing the simulation results while the ratio between α and β was fixed in [23], but the dynamics of the actuator were not considered in the design process. Kawai et al. [21] designed the frequency weighting filter for one of the state variables using a first-order low-pass filter. However, the parameters of the filter were not determined based on actuator dynamics but were manually tuned without a clear explanation of the parameter selection process (Fig. 4).

We propose a systematic method to determine the parameters α and β based on the actuator dynamics by analyzing its frequency response. The inverse of the weighting function, $R_f(j\omega)^{-1}$, is designed as a low-pass filter with the same cutoff frequency as the frequency response of the fan, as follows:

$$\left|R_f(j\omega)^{-1}\right| = \sqrt{\frac{1+\beta^2 f_{cutoff}^2}{1+\alpha^2 f_{cutoff}^2}} = \frac{1}{\sqrt{2}} \tag{25}$$

where f_{cutoff} denotes the cutoff frequency of the actuator, which in our application is that of the fan. To determine the ratio between α and β, we utilize the stopband attenuation of the actuator M_{stop} from Fig. 3(b). M_{stop} is applied as the stopband attenuation of $R_f(j\omega)^{-1}$ when $\omega \to \infty$ as follows:

$$M_{stop} = 20\log_{10}(\beta/\alpha) \tag{26}$$

Substituting (26) into (25), we can determine $\alpha = 0.383$ and $\beta = 0.073$ for $M_{stop} = -14.30$ dB. In this way, input signals with frequencies lower than the cutoff frequency, which represent the practically usable bandwidth, are actively utilized, while frequencies higher than the cutoff frequency are penalized by $R_f(jw)$. Frequencies higher than M_{stop} are treated equally, as the actual response for this usually arises from sensor resolution limitations, noise, and backlash. This design framework can be extended to other systems with different actuator dynamics, as long as the actuators provide good tracking performance at low frequencies and their performance decreases as the frequency increases.

The developed standard quadratic cost function is solved using Sequential Quadratic Programming (SQP), which iteratively solves QP approximations while handling constraints. We implemented the nonlinear optimization-based control using the ACADO toolkit [27] and the QP solver qpOASES [28] (Fig. 4). We employed a Gauss–Newton Hessian approximation with multiple shooting and integrate the dynamics using a 4th order Runge Kutta (INT RK4) scheme with 50 steps. The prediction horizon was set to 0.3 s so that it can cover more than twice the time it takes for the pendulum to naturally fall down, for a sufficient prediction range considering its dynamics. Asymmetric thrust constraints of -2.35 N and 3.74 N were applied in the optimization process. This setting, including the asymmetric thrust constraint, was applied in both the simulations and experiments presented in the following sections. Thanks to the compact system with five states and two inputs, the solver could run within every millisecond, which is sufficient for real-time implementation.

IV. Simulational Analysis

Simulation studies were conducted to evaluate the sensitivity and stability of FSMPC with the proposed design framework. Formal stability guarantees for FSMPC in constrained nonlinear systems remain an open research challenge due to the complexity of nonlinearity, constraints, and discretization. Preliminary work by Yun et al. [22] provides a theoretical stability analysis of FSMPC; however, it is limited to linear time-invariant discrete-time systems. Furthermore, Anderson et al. [29] established improved robustness of frequency-shaped cost functions in

IEEE Robotics and Automation Letters (RA-L) paper, presented at ICRA 2026, Vienna, Austria. Cite as RA-L paper.

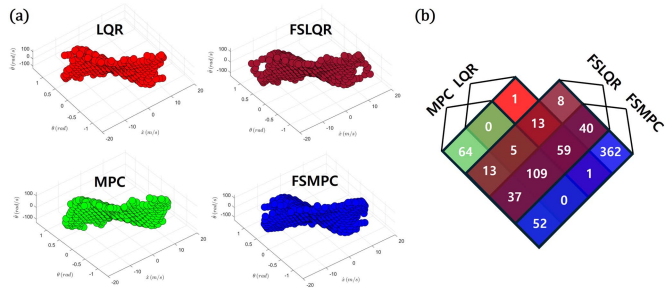

Fig. 5. Stability evaluation results. (a) Stability region obtained from the simulations. (b) Comparison of successful balancing cases among LQR, FSLQR, MPC, and FSMPC controllers, visualized as a Venn diagram.

Single-Input Single-Output (SISO) systems, but a formal proof for MIMO remains challenging. Therefore, we investigated the stability and robustness of the FSMPC through simulation analysis. The simulations utilized MuJoCo, a high-performance physics simulator widely used for dynamic systems modeling. A two-wheeled inverted pendulum system was designed and controlled in the sagittal plane. All system parameters, including states, inputs, and physical properties, were configured to align with the dynamics described in Section II, as well as the fan dynamics.

A. Stability Evaluation

The stability region was used to evaluate the stability of the proposed FSMPC in comparison to the conventional controllers LQR, MPC, and frequency shaped LQR (FSLQR), by comparing their balancing performance under various initial conditions. The MPC used for comparison is a standard nonlinear MPC that uses the same solver and settings as FSMPC, but without any frequency-shaped cost. The frequency cost of FSLQR was determined using the same strategy as FSMPC. The initial states, including linear velocity ($\dot{x}_0$), pitch angle (θ_0), and pitch angular velocity ($\dot{\theta}_0$), were varied across 30 evenly spaced levels, resulting in a total of 27,000 cases for each controller. For each case, the simulation ran for 10 seconds, with the system attempting to maintain balance throughout. Each simulation result was evaluated against failure thresholds of $\dot{x} = 0.2$ m/s, $\theta = 0.04$ rad, and $\dot{\theta} = 0.4$ rad/s, and it was considered successful if the system maintained balance for two seconds after 8s without exceeding any of these thresholds. The results of the simulations are shown in Fig. 5. FSMPC outperformed the other controllers, achieving 660 successful cases, which is more than two times the number of successful cases for LQR (188), FSLQR (284) and MPC (280). There are some cases where FSMPC fails while LQR, FSLQR or MPC succeeds. These cases typically occur under extreme initial conditions, such as when slip occurs or when the wheel lifts off the ground due to high initial wheel and body speed. These extreme conditions introduce significant modeling uncertainties; however, FSMPC achieves superior stability under such conditions by incorporating frequency-domain considerations about the actuator into its optimization process, outperforming other controllers. These results indicate that FSMPC provides enhanced stability under various conditions.

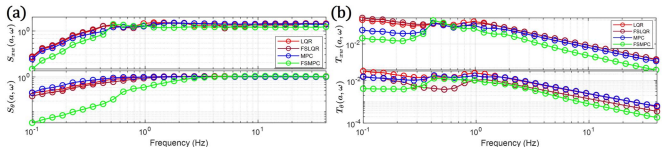

Fig. 6. Generalized sensitivity function $S(a,\omega)$ and complementary sensitivity function $T(a,\omega)$ for LQR, FSLQR, MPC, and FSMPC. (a) Sensitivity with respect to a sinusoidal reference: x_w in the upper subplot with amplitude $a = 0.1$, and θ in the lower with $a = 0.01$. (b) Complementary sensitivity with respect to a sinusoidal disturbance with amplitude $a = 0.1$.

B. Generalized Sensitivity Analysis

To further investigate the stability and robustness of the system, a frequency-domain sensitivity analysis was performed. While classical sensitivity theory applies limited to linear time-invariant systems, Pavlov et al. [30] extended it to nonlinear systems by defining the generalized sensitivity function $S(a,\omega)$ and generalized complementary sensitivity function $T(a,\omega)$ as follows:

$$S(a,\omega) = \frac{\|\bar{e}_{a\omega}\|_2}{\|r_{a\omega}\|_2}, T(a,\omega) = \frac{\|\bar{p}_{a\omega}\|_2}{\|r_{a\omega}\|_2} \tag{27}$$

where $r_{a\omega}(t) = a\sin(\omega t)$ is a sinusoidal reference trajectory of amplitude a and frequency ω, $\bar{e}_{a\omega}(t)$ its steady-state output error, and $\bar{p}_{a\omega}(t)$ is steady-state output. Although a formal theorem linking the generalized sensitivity function to the stability of nonlinear systems has not yet been established, the behavior of these functions can still provide valuable insights into system stability. In this analysis, we set $S(a,\omega)$ to $\bar{e}_{a\omega}(t)$ of x_w and θ induced by the sinusoidal reference $r_{a\omega}(t)$ of the corresponding variable. $T(a,\omega)$ was set to $\bar{p}_{a\omega}(t)$ of x_w and θ induced by the sinusoidal disturbance $r_{a\omega}(t)$ applied to the right side of both (8) and (9).

Fig. 6(a) shows the generalized sensitivity function $S(a,\omega)$. FSMPC reduces $S(a,\omega)$ across the low-frequency region compared to LQR, FSLQR, and standard MPC, indicating superior tracking performance and disturbance rejection. FSMPC also shows improved generalized complementary sensitivity function $T(a,\omega)$ across the high-frequency region (Fig. 6(b)), demonstrating robustness against high frequency disturbances such as unmodeled fan dynamics, wheel slip, and measurement noise. Although the formal stability analysis of nonlinear FSMPC remains an open problem, these simulation results imply that the system exhibits stable and robust characteristics.

V. Experimental Validation

The FSMPC was tested with the WIPF prototype shown in Fig. 2.

A pendulum-like load with variable mass was used to apply controlled impacts to the WIPF body to verify the impact robustness of the system. The drop height was set to 0.38 m, ensuring consistent and reproducible impact forces across all trials. The first experiment was performed with a 0.6 kg load. As shown in Fig. 7(a) and the attached video, the FSMPC achieved the smallest wheel displacement with a wheel travel of 0.20 m

IEEE Robotics and Automation Letters (RA-L) paper, presented at ICRA 2026, Vienna, Austria. Cite as RA-L paper.

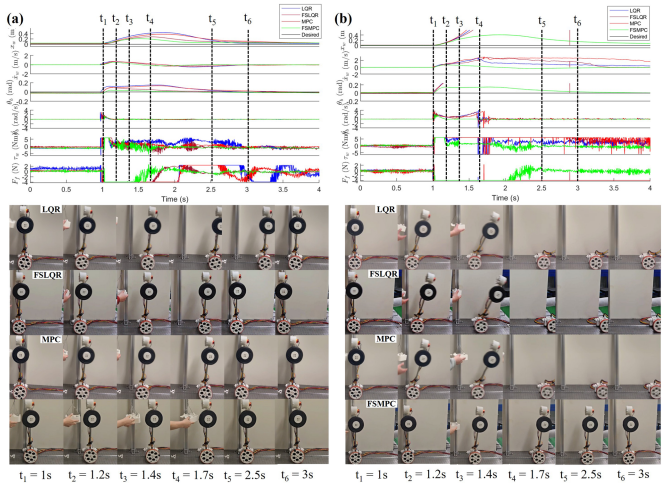

Fig. 7. Impact robustness test results. (a) Motion of the WIPF system over time when a 0.6 kg load was applied to the COM of the body. (b) Motion of the WIPF system over time when a 1.1 kg load was applied to the COM of the body.

and a pitch change of 0.037 rd, while LQR, FSLQR and MPC exhibited larger deviations (0.435 m and 0.148 rd for LQR, 0.276 m and 0.0980 rd for FSLQR, 0.374 m and 0.13 rd for MPC). When the load was increased to 1.1 kg (Fig. 7(b) and the attached video), LQR, FSLQR and MPC failed to maintain balance, whereas FSMPC stabilized the system with a maximum wheel deviation of 0.41 m and a pitch change of 0.14 rad. The results suggest that the actuator dynamics-aware FSMPC design significantly enhances the balancing performance under external disturbances. The improved performance of FSMPC arises from its frequency-shaped cost design, which explicitly accounts for the actuator's limited bandwidth. Unlike LQR and standard MPC, which do not utilize the actuator dynamics, FSMPC puts penalty on high-frequency control actions through the proposed weighting filter design. FSMPC also shows better performance than FSLQR, as it can explicitly accounts for the asymmetric input constraint. The typical average calculation time of the FSMPC solver was about 600 μs, which was sufficient for these real-time experiments.

VI. Conclusion

In this research, we proposed a frequency-aware design framework for FSMPC to control the WIPF system, which has a small actuator force bandwidth. The dynamics of the fan providing bidirectional thrust was identified, and the cost function of FSMPC was designed by incorporating the actuator dynamics. The stability and robustness of the proposed FSMPC was evaluated through both simulations and experiments, and compared against LQR, standard MPC, and FSLQR controllers that do not explicitly account for fan dynamics or input constraints. The results demonstrate that FSMPC achieves improved stability and robustness compared to other controllers. The mathematical stability analysis and proof remain open problems. However, the FSMPC with the proposed design framework can be extended to other systems that require consideration of slow actuators, such as pneumatic actuators and low-stiffness series elastic actuators. Future research will focus on a two-wheeled WIPF robot with two linear legs, which will require a higher computational burden for FSMPC due to the increased number of states.

Acknowledgment

The authors utilized ChatGPT to improve the clarity and readability of the manuscript. All intellectual contributions remain solely those of the authors.

References

[1] H. Nguyen et al., "Segway robotic mobility platform," *,Proc SPIE*, vol. 5609, pp. 207–220, 2004.
[2] M. Sasaki, N. Yanagihara, O. Matsumoto, and K. Komoriya, "Steering control of the personal riding-type wheeled mobile platform (PMP)," in *Proc. IEEE/RSJ Int. Conf. Intell. Robots Syst.*, 2005, pp. 1697–1702.
[3] J. Huang, F. Ding, T. Fukuda, and T. Matsuno, "Modeling and velocity control for a novel narrow vehicle based on mobile wheeled inverted pendulum," *IEEE Trans. Control Syst. Technol.*, vol. 21, no. 5, pp. 1607–1617, Sep. 2013.
[4] Y. Xin, H. Chai, Y. Li, X. Rong, B. Li, and Y. Li, "Speed and acceleration control for a two wheel-leg robot based on distributed dynamic model and whole-body control," *IEEE Access*, vol. 7, pp. 180630–180639, 2019.
[5] G. Krishna, D. Sumith, and G. Akshay, "Epersist: A two-wheeled self-balancing robot using PID controller and deep reinforcement learning," in *Proc. 22nd Int. Conf. Control, Automat. Syst.*, Nov. 2022, pp. 1488–1492.
[6] V. Klemm et al., "Ascento: A two-wheeled jumping robot," in *Proc. IEEE Int. Conf. Robot. Automat.*, 2019, pp. 7515–7521.
[7] X. Li, H. Zhou, H. Feng, S. Zhang, and Y. Fu, "Design and experiments of a novel hydraulic wheel-legged robot," in *Proc. IEEE/RSJ Int. Conf. Intell. robots Syst.*, 2018, pp. 3292–3297.
[8] H. Chen, B. Wang, Z. Hong, C. Shen, P. Wensing, and W. Zhang, "Underactuated motion planning and control for jumping with wheeled-bipedal robots," *IEEE Robot. Automat. Lett.*, vol. 6, no. 2, pp. 747–754, Apr. 2021.
[9] J. Lee, H. Shin, S. Lee, and S. Jung, "Balancing control of a single-wheel inverted pendulum system using air blowers: Evolution of mechatronics capstone design," *Mechatronics*, vol. 23, pp. 926–932, 2013.
[10] B. Lee and S. Jung, "Design, control and experiment of two-wheel transform robot," *J. Inst. Electron. Inf. Engineers*, vol. 60, pp. 58–65, 2023.
[11] S. Larimi, P. Zarafshan, and S. Moosavin, "A new stabilization algorithm for a two-wheeled mobile robot aided by reaction wheel," *J. Dynamic Systems, Measurement, Control*, vol. 137, no. 1, 2015, Art. no. 011009.
[12] J. Park and B. Cho, "Development of a self-balancing robot with a control moment gyroscope," *Int. J. Adv. Robotic Syst.*, vol. 15, pp. 1–11, 2018.
[13] D. Kim and Y. Jung, "A wheeled inverted pendulum with a fan for enhanced balancing," *J. Korean Soc. Mech. Technol.*, vol. 26, no. 1, pp. 34–44, 2024.
[14] E. Sihite, A. Kalantari, R. Nemovi, A. Ramezani, and M. Gharib, "Multimodal mobility Morphobot(M4) with appendage repurposing for locomotion plasticity enhancement," *Nature Commun.*, vol. 14, pp. 1–15, 2023.
[15] M. Bjelonic, R. Grandia, O. Harley, C. Galliard, S. Zimmermann, and M. Hutter, "Whole-body MPC and online gait sequence generation for wheeled-legged robots," in *Proc. IEEE/RSJ Int. Conf. Intell. robots Syst.*, 2020, pp. 8388–8395.
[16] F. Nan, S. Sun, P. Foehn, and D. Scaramuzza, "Nonlinear MPC for quadrotor fault-tolerant control," *IEEE Robot. Automat. Lett.*, vol. 7, no. 2, pp. 5047–5054, Apr. 2022.
[17] B. Lindqvist, S. Mansouri, A. Agha-mohammadi, and G. Nikolakopoulos, "Nonlinear MPC for collision avoidance and control of UAVs with dynamic obstacles," *IEEE Robot. Automat. Lett.*, vol. 5, no. 4, pp. 6001–6008, Oct. 2020.
[18] Z. Wang, J. Li, and D. duan, "Manipulation strategy of tilt quad rotor based on active disturbance rejection control," *Proc. Inst. Mech. Engineers, Part G, J. Aerosp. Eng.*, Vol. 234, no. 3, pp. 4301–4306, 2020.
[19] M. Jacquet, G. Corsini, D. Bicego, and A. Franchi, "Perception-constrained and motor-level nonlinear mpc for both underactuated and tilted-propeller uavs," in *Proc. IEEE Int. Conf. Robot. Automat.*, 2020, pp. 4301–4306.
[20] N. Gupta, "Frequency-shaped cost functionals—Extension of linear-quadratic-Gaussian design methods," *J. Guid. Control*, vol. 3, no. 6, pp. 529–535, 1980.

[21] Y. Kawai and K. Uchiyama, "Design of frequency shaped LQR considering dynamic characteristics of the actuator," in *Proc. Int. Conf. UnmannedAircr. Syst.*, 2016, pp. 1235–1239.

[22] H. Yun, H. Chang, H. Shim, and J. Seo, "A preliminary result on frequency-shaped model predictive control," in *Proc. 2015 54th IEEE Conf. Decis. Control*, Dec. 2015, pp. 2395–2399.

[23] R. Grandia, F. Farshidian, A. Dosovitskiy, R. Ranftl, and M. Hutter, "Frequency-aware model predictive control," *IEEE Robot. Automat. Lett.*, vol. 4, no. 2, pp. 1517–1524, Apr. 2019.

[24] C. Peng and C. Su, "Modeling and parameter identification of a cooling fan for online monitoring," *IEEE Trans. Instrum. Meas.*, vol. 70, 2021, Art. no. 3522914.

[25] E. Johnson and M. Turbe, "Modeling, control, and flight testing of a small-ducted fan aircraft," *J. Guid., Control, Dyn.*, vol. 29, no. 4, pp. 769–779, 2006.

[26] ODrive Robotics, "ODrive," 2020. Accessed: May 12, 2025. [Online]. Available: https://odriverobotics.com

[27] B. Houska, H. Ferreau, and M. Diehl, "ACADO toolkit—An open-source framework for automatic control and dynamic optimization," *Optimal Control Appl. Methods*, vol. 32, no. 3, pp. 298–312, 2011.

[28] H. Ferreau, C. Kirches, A. Potschka, H. Bock, and M. Diehl, "qpOASES: A parametric active-set algorithm for quadratic programming," *Math. Program. Computation*, vol. 6, pp. 327–363, 2014.

[29] B. Anderson and D. Mingori, "Use of frequency dependence in linear quadratic control problems to frequency-shape robustness," *J. Guid., Control, Dyn.*, vol. 8, no. 3, pp. 397–401, 1985.

[30] A. Pavlov, N. van de Wouw, A. Pogromsky, M. Heertjes, and H. Nijmeijer, "Frequency domain performance analysis of nonlinearly controlled motion systems," in *Proc. 46th IEEE Conf. Decis. Control*, 2007, pp. 1621–1627.